Powder Technology 427 (2023) 118710

Contents lists available at ScienceDirect

Powder Technology

journal homepage: www.journals.elsevier.com/powder-technology

Exploring the role of nasal hair in inhaled airflow and coarse dust particle dynamics in a nasal cavity: A CFD-DEM study

Ahmadreza Haghnegahdar [a], Rahul Bharadwaj [a], Yu Feng [b,*]

[a] ANSYS Inc, Waltham, MA 02451, USA
[b] School of Chemical Engineering, Oklahoma State University, Stillwater, OK 74078, USA

HIGHLIGHTS

- A new CFD-DEM model is developed to simulate interactions between nasal hairs and inhaled air-particle flow.
- Nasal hair presence is crucial for accurate particle deposition predictions.
- Increasing nasal hair diameter decreases filtration efficiency for 5–7 μm particles but increases it for 7–15 μm particles.
- Nasal hairs are more efficient in filtering small particles than large particles.

GRAPHICAL ABSTRACT

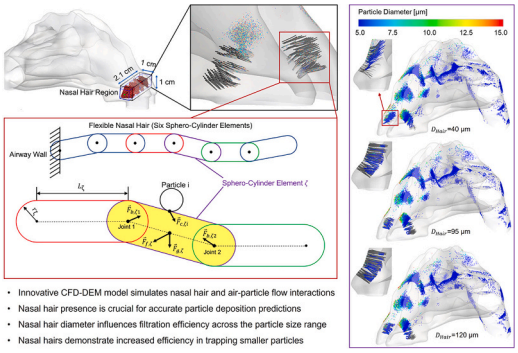

ARTICLE INFO

Keywords:
Nasal hair
Flexible fiber
Bonded sphero-cylinder model
Discrete element method (DEM)
Computational fluid dynamics (CFD)
Inhaled air-particle flow dynamics

ABSTRACT

This study presents a novel coupled computational fluid dynamics-discrete element method (CFD-DEM) model for simulating airflow and inhaled particle dynamics in the nasal cavity, considering the fluid-structure interactions between nasal hair and airflow, which are often overlooked in existing CFD simulations. The CFD-DEM model, based on a virtual nasal cavity geometry, represents nasal hairs as flexible fibers implanted on the inner wall of the nasal cavity. Inhaled air-particle transport dynamics were simulated in the presence of nasal hairs with three different diameters (40, 95, and 120 μm), and the results were compared with simulations without nasal hairs. Polydisperse particles with diameters ranging from 5 to 15 μm, aligning with global coarse dust statistics, were inhaled at flow rates between 216 mL/s and 630 mL/s, representing human nose breathing conditions from rest to exercise. The CFD-DEM simulation results indicate that the differences in deposition fraction predictions between cases with and without nasal hairs exceed 20% for particle size ranges corresponding to impaction parameter values between 3E+3 and 2E+4 $\mu m^2 cm^3/s$. This emphasizes the importance of accounting for nasal hair interactions in accurately simulating inhaled particle transport dynamics within the nasal cavity. Thinner nasal hairs, more flexible than thicker ones, lead to more significant deformation and allow more particles to penetrate the nasal vestibule without being trapped. Additionally, thinner hairs occupy a smaller cross-section area in the nasal vestibule, resulting in lower filtration capability due to decreased particle deposition from interception and inertial impaction. Thicker nasal hairs trap more coarse dust particles (> 5 μm) effectively than thinner nasal hairs. Moreover, as the nasal hair diameter increases, particle deposition on the

* Corresponding author at: 420 Engineering North, Stillwater, OK 74078, USA.
E-mail address: yu.feng@okstate.edu (Y. Feng).

https://doi.org/10.1016/j.powtec.2023.118710
Received 11 April 2023; Received in revised form 19 May 2023; Accepted 5 June 2023
Available online 9 June 2023

nasal cavity wall decreases. Nasal hairs demonstrate higher efficiency in trapping smaller particles. In conclusion, the CFD-DEM model, capable of modeling nasal hair motion, can serve as a next-generation in silico tool for investigating biofluid dynamics in the nasal cavity.

1. Introduction

Nasal hairs, also known as vibrissae, are present in the nostrils of adult humans and play a crucial role in filtering inhaled particulate matter (PM) and collecting moisture [1]. Since pulmonary diseases are relevant to the deposition location and dose of inhaled toxic particulate matters, the presence of the nasal hairs (see Fig. 1) and their filtration capability on those respirable particles [2], which will have influences on the pulmonary disease progression and should be studied.

Unfortunately, such impacts of these nasal hairs have not been fully understood. There are only a few existing in vitro and in vivo studies on nasal hair property measurements and their influence on inhaled particle filtration and pulmonary diseases [1–5]. Specifically, Pham et al. [1] quantify the number of nasal hairs in the right and left nostril in healthy controls and measure the distance of nasal hair growth distally to proximally in 20 cadavers with a mean age of 83. They found the average nasal hair counts are approximately 120 and 122.2 in the left and right nostrils, respectively. The distance from the nostril opening to the deepest location where nasal hair grows (i.e., the depth of the nasal hair region in the nostrils) ranges from 0.81 cm to 1.035 cm. Based on clinical studies, Ozturk et al. [2] found that amount of nasal hair providing a nose filtration function has a protective effect on the risk of developing asthma in seasonal rhinitis patients. Stoddard et al. [3] investigated the relationship between nasal hair density and the nasal obstruction based on the subjective and objective assessments of 30 volunteers. Ma [4] constructed an in vitro nasal valve model and measured the nasal hair trapping efficiency on particles from 2 to 5 μm under breathing conditions from rest to exercise. The study [4] indicates that thinner nasal hair with smaller hair diameters can block 2-to-5 μm particles and particles <0.01 μm more efficiently. However, Prinz and Murray [5] measured the nasal hair-to-dermis detachment in humans and quantified the pullout force required in adult males. They found nasal hair thickness (i.e., diameter) is unrelated to required pullout force.

Other than the above-mentioned in vitro and in vivo studies, in silico studies based on computational fluid particle dynamics (CFPD) have been widely employed for simulating the airflow and inhaled particle dynamics in the nasal cavity [6–13]. Specifically, multiphase flow models, such as the Euler-Lagrange models, are emerging as powerful digital tools in otolaryngology. These models [6–13] contribute significantly to the advancement of fundamental understanding and improved clinical treatment outcomes for various upper airway diseases, including nasal airway obstruction [14], chronic rhinosinusitis [15], empty nose syndrome [16], and laryngotracheal stenosis [17]. However, current CFPD research efforts cannot explicitly simulate the fluid-structure interactions between nasal hair and air-particle flow. As a simplification, these models often neglect the presence of nasal hair. This limitation is partly due to the constraints of the Euler-Lagrange model, which treats the discrete phase (e.g., nasal hairs) as mass points, and is unable to model the fiber-like shape effect and flexibility. Only one computational study has considered the presence of nasal hair [18], utilizing a porous-media model. Consequently, the impact of this simplification on the prediction of inhaled airflow fields and particle deposition distribution remains uncertain.

Therefore, based on the literature review, a comprehensive and systematic investigation of the influence of nasal hair properties (i.e., diameters) on inhaled particle transport dynamics and nasal filtration efficiency has yet to be conducted [19]. To fill the knowledge gap and computational modeling deficiency mentioned above, this study developed a hybrid computational model based on coupled computational fluid dynamics (CFD) and discrete element method (DEM) to simulate the interactions between the nasal hairs, airflow, and inhaled particles representing the global coarse dust, as a case study. It is worth noting that computational aerosol dynamics in human respiratory systems has greatly benefited from employing CFD-DEM because of its unique capability of modeling particle-particle and particle-wall interactions

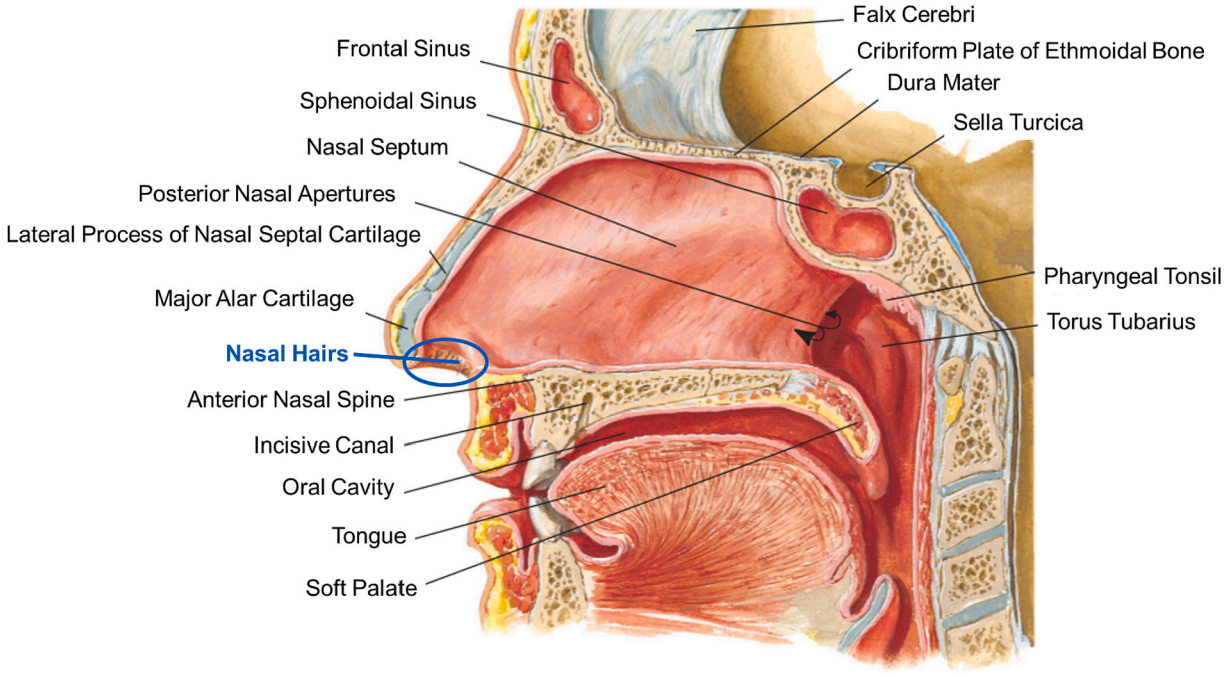

Fig. 1. Anatomy of the nasal cavity with indicated locations of nasal hair growth [61].

and non-spherical particle transport and interactions [20–22]. Specifically, employing the bonded flexible fiber model in DEM [23], each nasal hair was modeled using six bonded sphero-cylinder elements (see Fig. 2). Using this more physiologically realistic CFD-DEM model, simulations were performed in a subject-specific nasal cavity geometry (see Fig. 2) to investigate how nasal hair geometric features, particle size, and inhalation flow rate can influence the transport and deposition of inhaled PM thorough nasal cavity. This study also focused on quantifying the filtration capability of nasal hair presence, and study on whether neglecting nasal hairs in CFPD simulations will lead to noticeable difference in aerosol transport dynamics predictions in human nasal cavity.

To address the knowledge gap and computational modeling limitations mentioned earlier, this study developed a hybrid computational model, coupling CFD and discrete element method (DEM), to simulate the interactions between nasal hairs, airflow, and inhaled particles, using global coarse dusts [24] larger than 5 μm as a case study. Specifically, the bonded flexible fiber model in DEM [23] was employed, modeling each nasal hair with six bonded sphero-cylinder elements (see Fig. 2). By utilizing this more physiologically realistic CFD-DEM model, simulations were conducted in a subject-specific nasal cavity geometry (see Fig. 1) to examine how nasal hair geometric features, particle size, and inhalation flow rate influence the transport and deposition of inhaled particulate matter (PM) within the nasal cavity. Additionally, this study aimed to quantify the filtration capability of the nasal hair presence and determine whether neglecting nasal hairs in computational fluid-particle dynamics (CFPD) simulations results in significant inaccuracies in predicting aerosol transport dynamics within the human nasal cavity.

2. Methodology

2.1. Geometry and mesh

2.1.1. Nasal cavity geometry with nasal hairs

The subject-specific nasal cavity geometry used in this study is shown in Fig. 2. Specifically, the geometry represents the nasal passage of a healthy 53-year-old, non-smoking male widely used by other numerical studies [11–13,25]. Nasal hairs were placed near the nostrils with physiological realism (see Figs. 1 and 2). Specifically, the nasal hair is composed of six sphero-cylinder elements, the first of which is frozen and attached to the nasal cavity wall surface. Measurements in a cadaveric population [1] show that the depth of the nasal hair region in nostrils is from 0.81 cm to 1.035 cm. Therefore, cell centers and surface normal of the CFD mesh at a 1 cm × 1 cm × 2.1 cm cubical region inside the vestibule nostrils have been extracted using a user-defined function (UDF) compiled in Ansys Fluent 2022 R1 (Ansys Inc., Canonsburg, PA) (see Appendix A). The selected region has a total surface area of 131.2 mm^2, and the number of surface mesh elements contributes to approximately 131 equally spaced strands in each nasal vestibule. This is in line with the nasal hair growth area explained in [1,5]. The in vitro study planted nasal hairs in the artificial nostrils with a depth of 2 cm [5]. Using the aforementioned information and the physiology of the nasal hairs, the length of the hair strands is assumed to be 0.3 cm. The center of mass and initial orientation of each hair strand are determined accordingly.

2.1.2. Mesh independence test

A mesh independence test was conducted to find the optimal balance between computational efficiency and accuracy. Four unstructured polyhedron-based finite volume meshes were generated using Ansys Fluent Meshing 2020 R2 (Ansys Inc., Canonsburg, PA, USA) with 5 near-wall prism layers to accurately capture boundary layer flow regimes and laminar-to-turbulence transition sites. The details of the four meshes (i.e., Mesh 1 to Mesh 4), which have increasing levels of refinement, are

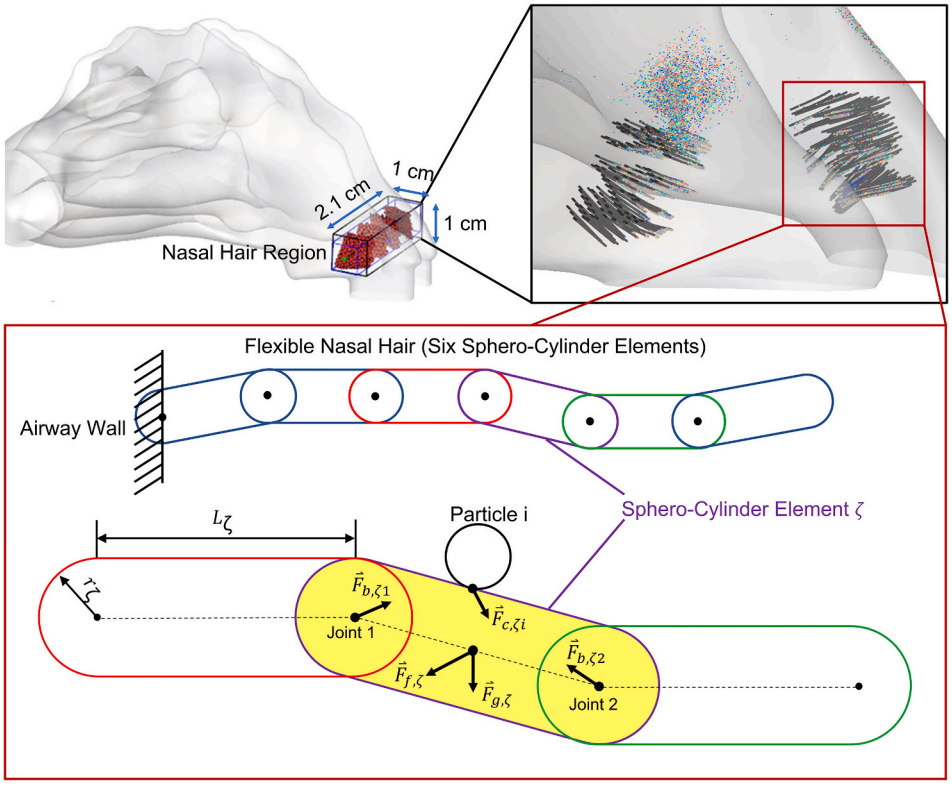

Fig. 2. Schematic of the nasal hair region and the 6-element flexible fiber model describing the nasal hair motion using the discrete element method (DEM).

shown in Table 1 as well as Fig. 3. Velocity magnitudes at 50 selected monitor points in the computational domain was recorded and compared between the simulation results using the 4 meshes. The percentage differences between the more refined meshes and the less refined ones were calculated. Among the 50 monitor points (see Fig. 3 (a)), the largest velocity difference between meshes decreased as mesh refinement increased. As shown in Fig. 3 (b), the average velocity difference across all 50 points between Mesh 3 and Mesh 4 was 2.34%, falling below the 5% threshold for the first time with mesh refinement. Consequently, further refinement from Mesh 3 to Mesh 4 did not significantly impact the flow field prediction, indicating that Mesh 3 provided the best balance between computational accuracy and efficiency. Thus, Mesh 3 was chosen as the final mesh, comprising 901,781 cells, 4,257,745 faces, and 2,650,848 nodes. Mesh 3 details can be found in Figs. 3 (c) and (d).

2.2. Governing equations

2.2.1. Discrete element method (flexible fiber model) for nasal hair dynamics

Discrete Element Method (DEM) is a computational model capable of explicitly modeling the interactions between particles with arbitrary shapes [26]. Force and moment balance equations are solved for each particle to determine its translational and rotational motions. Based on the classical DEM modeling framework, bonded sphero-cylinder flexible fiber model [16] was developed (see Fig. 2) which has been validated to be able to simulate motions of flexible fibers in DEM modeling scheme. To model nasal hairs as flexible fibers, each hair was represented by an assembly of six sphero-cylinder elements (see Fig. 2). Each sphero-cylinder element is assumed to be rigid, with connections at the center points of the hemispherical cap surfaces at both ends of an element, referred to as joints. No breakage is assumed between these elements at the joints for the nasal hair in this study. The joints are characterized by a linear elastic model without plastic deformation, where force and moment are directly proportional to the linear or angular joint deformation, respectively. To account for the hardness of the hair fibers, the stiffness $K_{\zeta 1}$ and $K_{\zeta 2}$ of the joints (i.e., Joint 1 and Joint 2) at the two ends of the generalized sphero-cylinder element ζ relative to neighboring elements (see Fig. 2) is multiplied by 10 (see Table 2).

When simulating the dynamics of nasal hairs in the nasal cavity under the influence of inhaled airflows and particle interactions, Newton's second law of motion is applied to each sphero-cylinder element to determine the translational and angular acceleration, velocity, and displacement at the joints (see Fig. 1). The linear elastic plus viscous damping model is employed to represent the bonded forces and torques. Specifically, the force balance for the sphero-cylinder element ζ (see Fig. 1) can be expressed as

$$m_\zeta \frac{d\vec{u}_\zeta}{dt} = \sum_i \vec{F}_{c,\zeta i} + \vec{F}_{b,\zeta 1} + \vec{F}_{b,\zeta 2} + \vec{F}_{f,\zeta} + \vec{F}_{g,\zeta} \quad (1)$$

where m_ζ is the mass of sphero-cylinder element ζ, $\vec{u}_\zeta$ is the translational velocity of sphero-cylinder element ζ, and $\vec{F}_{g,\zeta}$ is the gravity of sphero-cylinder element ζ. $\vec{F}_{c,\zeta i}$ is the contact force acting on sphero-cylinder element ζ due to the collision with inhaled spherical particle i. $\vec{F}_{c,\zeta i}$ is calculated by employing the Hertz-Mindlin (H-M) Johnson-Kendall-Roberts (JKR) cohesion model [27,28]. The expression of $\vec{F}_{c,\zeta i}$ is identical to the contact force between inhaled particles $\vec{F}_{c,ji}$, which can be found in Section 2.2.2.2.

Moreover, $\vec{F}_{f,\zeta}$ in Eq. (1) represents the hydraulic force acting on the sphero-cylinder element, primarily attributed to drag force [29]. The Marheineke and Wegener drag rule is employed to calculate the drag force (i.e., $\vec{F}_{f,\zeta}$) on the sphero-cylinder elements of the flexible nasal hair fibers, considering both the normal and tangential components of the drag relative to the cylinder axis. To enhance convergence, a semi-implicit treatment is used for the coupling source terms on the CFD side. In this approach, the drag force is divided into explicit and implicit components by separating the unperturbed fluid velocity and the velocity at the geometric center of the sphere-cylinder element. Further details on the drag force can be found in [21].

Additionally, $\vec{F}_{b,\zeta 1}$ and $\vec{F}_{b,\zeta 2}$ in Eq. (1) are the bond forces induced by the bond deformation at Joint 1 and Joint 2 (see Fig. 2), i.e.,

$$\vec{F}_{b,\zeta 1} = K_{\zeta 1}\vec{\delta}_{rel,\zeta 1} + C_{\zeta 1}\frac{d\vec{\delta}_{rel,\zeta 1}}{dt} \quad (2)$$

$$\vec{F}_{b,\zeta 2} = K_{\zeta 2}\vec{\delta}_{rel,\zeta 2} + C_{\zeta 2}\frac{d\vec{\delta}_{rel,\zeta 2}}{dt} \quad (3)$$

where $\vec{\delta}_{rel,\zeta 1}$ and $\vec{\delta}_{rel,\zeta 2}$ are the relative displacement vectors between the centers of hemispherical ends from the two bonded sphero-cylinders at Joint 1 and Joint 2, respectively. Specifically, the relative displacement vector $\vec{\delta}_{rel}$ measures the linear deformation of a joint brought on by the relative translational movement of the connected parts. $K_{\zeta 1}$ and $K_{\zeta 2}$ are stiffnesses at Joint 1 and Joint 2, which can be calculated as.

$$K_{\zeta 1} = K_{\zeta 2} = 10\frac{E_\zeta A_\zeta}{L_\zeta} \quad (4a \text{ and } b)$$

where E_ζ is the Young's modulus of sphero-cylinders, $A_\zeta = \pi r_\zeta^2$ is the cross-section area of the cylinder, and L_ζ is the length of the cylinder. In Eqs. (2) and (3), $C_{\zeta 1}$ and $C_{\zeta 2}$ are damping coefficients.

The moment balance of sphero-cylinder ζ (see Fig. 2) around its mass center can be given as:

$$\bar{\bar{I}}_\zeta \frac{d\vec{\omega}_\zeta}{dt} = \begin{bmatrix} I_{\zeta,xx} & I_{\zeta,xy} & I_{\zeta,xz} \\ I_{\zeta,yx} & I_{\zeta,yy} & I_{\zeta,yz} \\ I_{\zeta,zx} & I_{\zeta,zy} & I_{\zeta,zz} \end{bmatrix} \begin{bmatrix} \frac{d\omega_{\zeta,x}}{dt} \\ \frac{d\omega_{\zeta,y}}{dt} \\ \frac{d\omega_{\zeta,z}}{dt} \end{bmatrix} = \sum_i \vec{M}_{c,\zeta i} + \vec{M}_{b,\zeta 1} + \vec{M}_{b,\zeta 1} \quad (5 \text{ a and b})$$

where $\bar{\bar{I}}_\zeta$ is the moment of inertia matrix which is a 2nd-rank tensor of the sphero-cylinder ζ, $\vec{\omega}_\zeta$ is the angular velocity vector, $\vec{M}_{c,\zeta i}$ is the contact torque induced by the tangential contact forces of particle i in contact with sphero-cylinder ζ, $\vec{M}_{b,\zeta 1}$ and $\vec{M}_{b,\zeta 1}$ are bond moment that arises from the bond forces $\vec{F}_{b,\zeta 1}$ and $\vec{F}_{b,\zeta 2}$ at Joint 1 and Joint 2 (see Fig. 2). It is worth mentioning that since $\vec{F}_{f,\zeta}$ and $\vec{F}_{g,\zeta}$ act at the center of mass of the sphero-cylinder, no torque is generated by them.

Bond forces ($\vec{F}_{b,\zeta 1}$ and $\vec{F}_{b,\zeta 2}$) and bond moments ($\vec{M}_{b,\zeta 1}$ and $\vec{M}_{b,\zeta 2}$) are meant to be the response to a combined entity that connects those places deforms at joints (see Fig. 2). The magnitude of the bond forces and moments at joints will depend on the angular and linear deformations, as well as on the deformation velocity in some cases.

It is worth mentioning that for sphero-cylinder elements which take over multiple CFD mesh cells, a Lagrange-Euler mapping is applied. An

Table 1
Mesh details for independence test.

Mesh No.	Cells	Faces	Nodes
Mesh 1	223,759	1,109,844	693,652
Mesh 2	460,068	2,208,313	1,278,989
Mesh 3 (Final)	901,781	4,257,745	2,650,848
Mesh 4	1,993,023	9,227,697	5,062,278

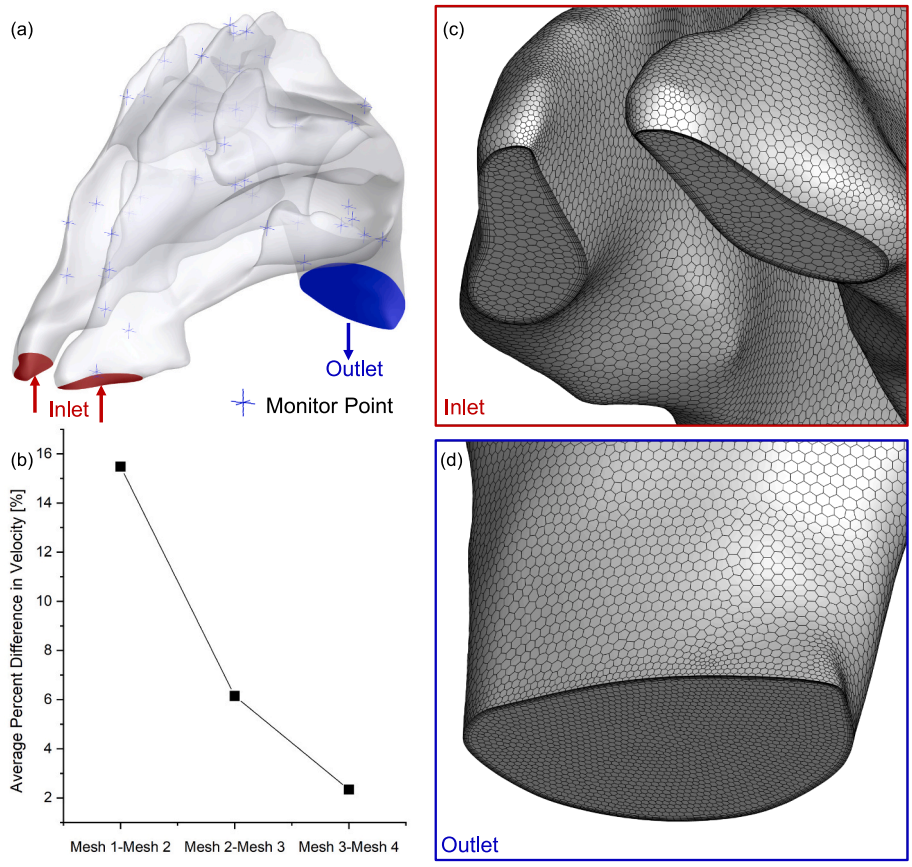

Fig. 3. Geometry, mesh independence test, and final mesh details of the subject-specific nasal cavity: (a) geometry and monitor points, (b) mesh independence test, (c) mesh details near the nasal inlets, and (d) mesh details near the outlet.

Table 2
Material properties of the particle groups in the CFD-DEM simulation.

Particle Group	Diameter [μm]	Length [cm]	Density [kg/m^3]	Young's Modulus [N/m^2]	Poisson's Ratio [−]	Number of Sphero-Cylinder Elements [−]	Elastic Ratio [−]	Damping Ratio [−]
Flexible Fibers (Nasal Hair)	40, 95, 120	0.3	1500	1E+07	0.3	6	1 (Isotropic)	1 (Joint and Element)
Spherical Particles (Inhaled PM)	5 (d_{50}) - 15 (d_{100})	N/A	1900	1E+07	0.3	N/A	N/A	N/A

Contact Pair	Static Friction Factor [−]	Dynamic Friction Factor [−]	Surface Energy [J/m^2]	Restitution Coefficient [−]
Spherical Particles - Spherical Particles	0.7	0.7	1.29	0.3
Spherical Particles - Flexible Fibers	0.5	0.5	1.29	0.3
Spherical Particles - Nasal Cavity	0.5	0.5	5	0.3
Flexible Fibers - Flexible Fibers	0.7	0.7	0	0.3
Flexible Fibers - Nasal Cavity	0.3	0.3	0	0.3

iterative discretized diffusion equation is implemented to calculate the exchanges of exceeding solid volume to the close neighboring cells during each iteration. These values are adjusted by automatically detecting optimal diffusion for each individual, and they are proportional to the value difference between the cell and its immediate neighbors.

2.2.2. *CFD-DEM for inhaled air-particle flow dynamics*

From a first principles perspective, CFD-DEM simulations aim to capture transport dynamics (i.e., analysis of spatio-temporal evolution) of inhaled particle laden airflow. Specifically, 3D nasal cavity that are discretized into finite volume mesh elements (see Fig. 3) are used to solve the pertinent governing equations including conservations of mass and momentum for continuous airflow, as well as force balance on each

inhaled particle.

2.2.2.1. Continuous phase (airflow). The airflow dynamics of the respiratory tract is always unsteady and driven by the pressure differences under the action of the cyclic breathing process. The conservation laws of mass and momentum can be written in tensor form as

$$\frac{\partial u_i}{\partial x_i} = 0 \tag{6}$$

$$\frac{\partial u_i}{\partial t} + u_j \frac{\partial u_i}{\partial x_j} = -\frac{1}{\rho}\frac{\partial p}{\partial x_i} + \frac{1}{\rho}\frac{\partial \tau_{ij}}{\partial x_j} + g_i \tag{7}$$

where u_j represents the fluid velocity, p is the pressure, $g_i = (9.81, 0, 0)$ [m/s^2] is gravity (standing position of human body), and viscous stress tensor τ_{ij} in Eq. (7) is given by

$$\tau_{ij} = \mu\left(\frac{\partial u_i}{\partial x_j} + \frac{\partial u_j}{\partial x_i}\right) \tag{8}$$

where μ is the air viscosity. Due to the laminar-to-turbulence transitional flow regime in the computational domain, the k-ω Shear Stress Transport (SST) model was employed in this study, which has been extensively validated in previous works [36–38].

2.2.2.2. Discrete phase (inhaled aerosol particles). Inhaled aerosol particles are assumed to be spherical. Neglecting the rotational motion of inhaled particles, translational motion equation was solved with the consideration of particle-particle and particle-nasal hair interaction. Specifically, the force balance of particle j can be given as

$$m_{p,j}\frac{d\vec{u}_{p,j}}{dt} = \sum_i \vec{F}_{c,ji} + \vec{F}_{fp,j} + \vec{F}_{g,j} \tag{9}$$

Here, $\vec{F}_{g,j}$ is the gravitational force. $\vec{F}_{fp,j}$ in Eq. (9) accounts for the fluid-particle interaction forces acting on particle j, i.e.,

$$\vec{F}_{fp} = \vec{F}_D + \vec{F}_{\nabla p} + \vec{F}_{VM} + \vec{F}_L + \vec{F}_{BM} \tag{10}$$

where $\vec{F}_D$ is the drag force [30,31], $\vec{F}_{\nabla p}$ is the pressure gradient force [32], $\vec{F}_{VM}$ is added (virtual) mass force [33], $\vec{F}_L$ is the Saffman lift force [34], and $\vec{F}_{BM}$ is the Brownian motion induced force [35]. The majority of these forces in Eq. (10) can be ignored. Specifically, since the density difference between fluid and particles is high ($\rho_p \gg \rho_f$), $\vec{F}_{VM}$ and $\vec{F}_L$ can be neglected. In addition, since the particle size is much smaller than the mesh cell size, $\vec{F}_{\nabla p}$ is negligible. It is also worth mentioning that the Cunningham correction factor [36] was included in the calculation of $\vec{F}_D$, of which the value ranges from 1.01 to 1.16 due to the aerosolized particle diameter simulated in this study.

In addition, $\vec{F}_{c,ji}$ in Eq. (9) denotes the contact force acting on particle j, induced by the interaction between particle i and particle j. It is worth noting that nasal hairs are also considered in the loop of particle i for contact detection and contact force calculation acting on particle j. In this study, the no-slip H-M model with the JKR cohesion model [27,28,37] was employed, i.e.,

$$\vec{F}_{c,ji} = \vec{F}^n_{c,ji} + \vec{F}^t_{c,ji} \tag{11}$$

Here, $\vec{F}^n_{c,ji}$ and $\vec{F}^t_{c,ji}$ are the normal and tangential contact force acting on particle j from particle i. $\vec{F}^n_{c,ji}$ can be described as a damped harmonic oscillator, which can be expressed as

$$\vec{F}^n_{c,ji} = \vec{F}^n_{e,ji} + \vec{F}^n_{d,ji} + \vec{F}^n_{adh,ji} \tag{12}$$

$$\vec{F}^t_{c,ji} = \vec{F}^t_{e,ji} + \vec{F}^t_{d,ji} + \vec{F}^t_{fr,ji} \tag{13}$$

In Eq. (12), $\vec{F}^n_{e,ji}$ is the normal elastic force, $\vec{F}^n_{d,ji}$ is the normal viscous damping force, and $\vec{F}^n_{adh,ji}$ is the adhesion force in the JKR cohesion model [28]. Specifically,

$$\vec{F}^n_{e,ji} = \left(K_n \delta^{\frac{3}{2}}_{nji}\right)\vec{n}_{ij} = \left(\frac{4}{3}E^*\sqrt{R^*}\,\delta^{\frac{3}{2}}_{nji}\right)\vec{n}_{ij} \tag{14 a and b}$$

$$\vec{F}^n_{d,ji} = \left(C_{nji}\delta^{\frac{1}{4}}_{nji}\dot{\delta}_{nji}\right)\vec{n}_{ij} = \left(\eta_{nji}\sqrt{5m^*K_n}\,\delta^{\frac{1}{4}}_{nji}\dot{\delta}_{nji}\right)\vec{n}_{ij} \tag{15 a and b}$$

$$\vec{F}^n_{adh,ji} = \sqrt{8\pi\Gamma E^* a^3}\,\vec{n}_{ij} \tag{16}$$

where δ_{nji} is the normal overlap distance between contacting particle i and particle j, K_n is the normal stiffness, $\vec{n}_{ji}$ is the unit normal vector, a is the radius of contact between particles or between a particle and a boundary [21], E^* is the effective Young's Modulus, R^* is the effective radius, $C_{nji} = \eta_{nji}\sqrt{5m^*K_n}$ is the normal damping coefficient, m^* is the effective mass, Γ is the surface energy, and η_{nji} is the normal damping ratio for the Hertzian model. Expressions for some of the above-mentioned parameters are given as

$$E^* = \left(\frac{1-\sigma_i^2}{E_i} + \frac{1-\sigma_j^2}{E_j}\right)^{-1} \tag{17}$$

$$\frac{1}{R^*} = \begin{cases} \dfrac{2}{d_{p,i}} + \dfrac{2}{d_{p,j}} & \text{particle j} - \text{particle i contact} \\ \dfrac{2}{d_{p,j}} & \text{particle j} - \text{boundary contact} \end{cases} \tag{18 a and b}$$

$$\frac{1}{m^*} = \begin{cases} \dfrac{1}{m_{p,i}} + \dfrac{1}{m_{p,j}} & \text{particle j} - \text{particle i contact} \\ \dfrac{1}{m_{p,j}} & \text{particle j} - \text{boundary contact} \end{cases} \tag{19 a and b}$$

E_i and E_j are Young's modulus of the two contacting particles or the particle and the boundary. σ_i and σ_j are the Poisson's ratios of the two contacting particles. $d_{p,i}$ and $d_{p,j}$ are diameters of the contacting particles. $m_{p,i}$ and $m_{p,j}$ are the mass of the contacting particles. η_{nji} can be calculated by a revised correlation [38] based on the analytical relationship between the normal damping coefficient η_{nji} and the coefficient of restitution ε ($0 \le \varepsilon \le 1$) [39], i.e.,

$$\varepsilon = \begin{cases} exp\left[-\dfrac{\eta_{nji}}{\sqrt{1-\eta_{nji}^{\,2}}} \left(\pi - tan^{-1} \dfrac{2\eta_{nji}\sqrt{1-\eta_{nji}^{\,2}}}{1-2\eta_{nji}^{\,2}} \right) \right] & 0 \le \eta_{nji} < \dfrac{\sqrt{2}}{2} \\ exp\left(-\dfrac{\eta_{nji}}{\sqrt{1-\eta_{nji}^{\,2}}} tan^{-1} \dfrac{2\eta_{nji}\sqrt{1-\eta_{nji}^{\,2}}}{2\eta_{nji}^{\,2}-1} \right) & \dfrac{\sqrt{2}}{2} \le \eta_{nji} < 1 \\ exp\left(-\dfrac{\eta_{nji}}{\sqrt{\eta_{nji}^{\,2}-1}} ln \dfrac{\eta_{nji}+\sqrt{\eta_{nji}^{\,2}-1}}{\eta_{nji}-\sqrt{\eta_{nji}^{\,2}-1}} \right) & 1 \le \eta_{nji} \end{cases} \quad \text{(20 a, b, and c)}$$

where the restitution coefficient ε is the user input that represents the particle-particle or particle-boundary interactions.

In Eq. (13), $\vec{F}^{t}_{e,ji}$ is the tangential elastic force, $\vec{F}^{t}_{d,ji}$ is the tangential viscous damping force, and $\vec{F}^{t}_{fr,ji}$ is the tangential friction. $\vec{F}^{t}_{e,ji}$ can be calculated using the Mindlin-Deresiewicz model [40], i.e.,

$$\vec{F}^{t}_{e,ji} = -\mu_p \left\| \vec{F}^{n}_{c,ji} \right\| \left(1-\lambda^{\frac{3}{2}}\right) \frac{\vec{\delta}_{tji}}{\left\| \vec{\delta}_{tji} \right\|} + \eta_{\tau ji} \left(\frac{6\mu_p m^{*} \left\| \vec{F}^{n}_{c,ji} \right\|}{\left\| \vec{\delta}_{tji} \right\|_{max}} \right) \lambda^{\frac{1}{4}} \vec{v}_{pt,ji} \quad (21)$$

$$\lambda = \begin{cases} 1 - \dfrac{min\left(\left\| \vec{\delta}_{tji} \right\|, \left\| \vec{\delta}_{tji} \right\|_{max} \right)}{s_{\tau,max}} & \left\| \vec{\delta}_{tji} \right\| \le \left\| \vec{\delta}_{tji} \right\|_{max} \\ 0 & \left\| \vec{\delta}_{tji} \right\| > \left\| \vec{\delta}_{tji} \right\|_{max} \end{cases} \quad \text{(22 a and b)}$$

where μ_p is the friction coefficient, $\eta_{\tau ji}$ is the tangential damping ratio estimated, $\vec{\delta}_{tji}$ is the tangential relative displacement at the contact, $\vec{v}_{pt,ji}$ is the tangential component of the relative velocity vector between particle i and particle j, and $\left\| \vec{\delta}_{tji} \right\|_{max}$ is the maximum relative tangential displacement at which particles begin to slide. Specifically, μ_p can be given as.

$$\mu_p = \begin{cases} \mu_s & \text{no sliding at the contact} \\ \mu_d & \text{sliding at the contact} \end{cases} \quad \text{(23 a and b)}$$

in which μ_s and μ_d are the static and kinetic friction coefficients (see Table 2), respectively. The tangential damping ratio $\eta_{\tau ji}$ can be given as

$$\eta_{\tau ji} = \frac{ln\varepsilon}{\sqrt{ln^2\varepsilon + \pi^2}} \quad (24)$$

The value of the maximum relative tangential displacement $\left\| \vec{\delta}_{tji} \right\|_{max}$ can be determined by

$$\left\| \vec{\delta}_{tji} \right\|_{max} = \mu_p \left(\frac{1-\sigma_i}{2-\sigma_i} + \frac{1-\sigma_j}{2-\sigma_j} \right)^{-1} \delta_{nji}$$

$\vec{v}_{pt,ji}$ in Eq. (21) is defined as

$$\vec{v}_{pt,ji} = \left(\vec{v}_{p,ji} \times \vec{n}_{ji} \right) \times \vec{n}_{ji} = \vec{v}_{p,ji} - \vec{v}_{n,ji} \quad \text{(25 a and b)}$$

where $\vec{v}_{pn,ji}$ is the normal component of the relative velocity $\vec{v}_{p,ji}$ between particle i and particle j. $\vec{v}_{pn,ji}$ is defined as

$$\vec{v}_{pn,ij} = \left(\vec{v}_{p,ij} \cdot \vec{n}_{ij} \right) \vec{n}_{ij} \quad (26)$$

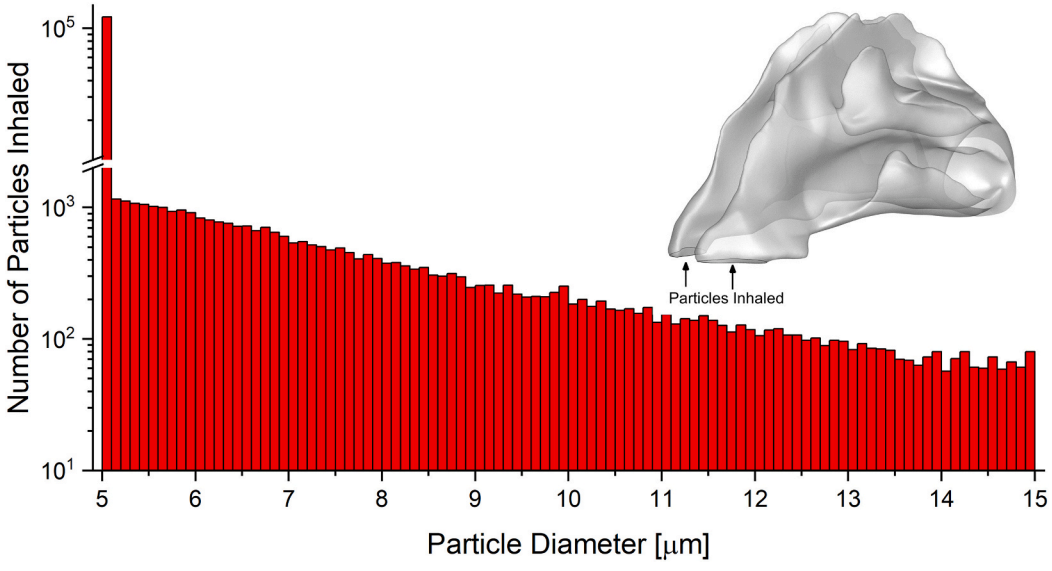

Fig. 4. Number of inhaled polydispersed particles.

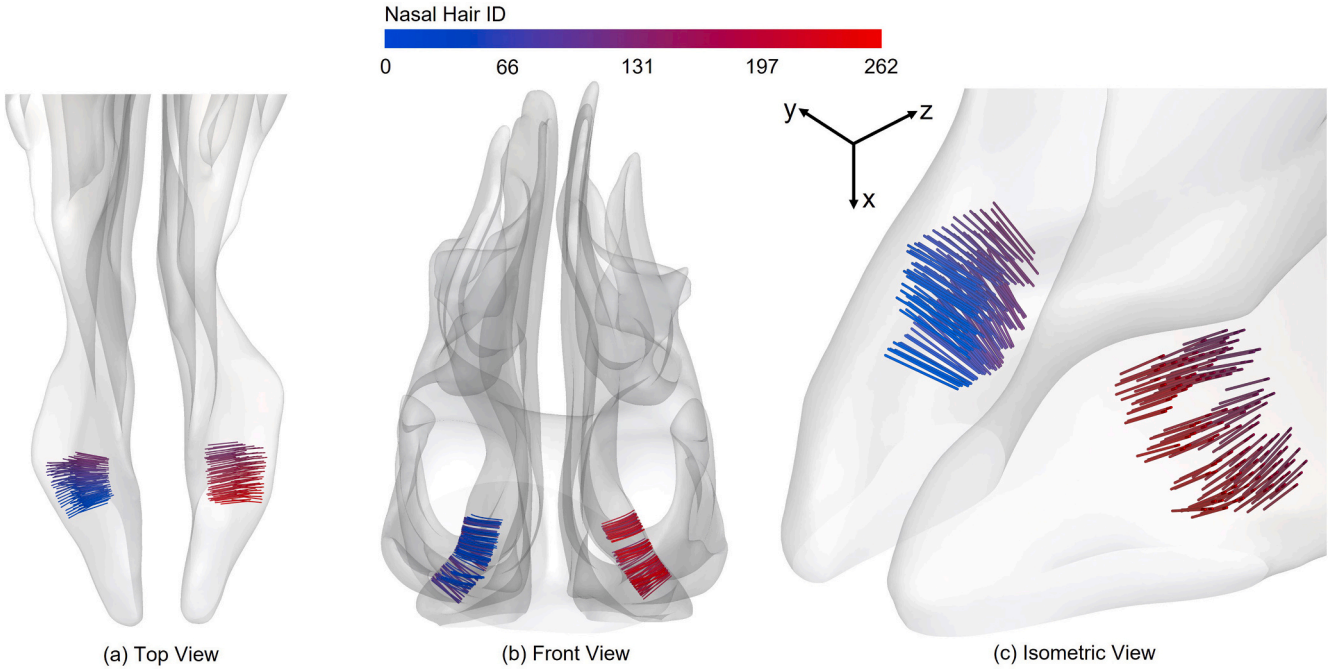

Fig. 5. Regions where the nasal hairs are being planted.

where $\vec{v}_{p,ji}$ is defined as

$$\vec{v}_{p,ij} = \vec{v}_{p,j} - \vec{v}_{p,i} \tag{27}$$

2.2.3. Particle deposition fraction (DF)

Particle deposition fraction (DF) is defined as the mass of deposited particles in a specific region divided by the total mass of particles entering the nostrils [41], i.e.,

$$DF = \frac{Deposited\ Particle\ Mass}{Total\ Particle\ Mass\ Inhaled} \tag{28}$$

2.3. Material properties

2.3.1. Inhaled particles

The CFD simulations performed in this study aim to simulate flow dynamics within a patient-specific nasal cavity, starting with a polydisperse aerosol size distribution (see Fig. 4). Inhaled particles are considered to have the size of typical coarse dust particles suspending in the air [24]. A polydisperse particle size distribution (PSD) is defined using Sieve Size approach, which matches the PSD of particles ranging from 5 μm to 15 μm of the global coarse dusts [24]. Fig. 4 shows the inhaled particle number vs. particle size employed in this study. $d_{p,50}$ = 5 μm and $d_{p,100}$ = 15 μm are the two data points on a semi-logarithmic plot of Cumulative Mass Percentage versus Sieve Size. The DEM solver uses a linear interpolation between these two points to define the size distributions of the inhaled particles. Table 2 provides information on the physical and interaction properties of the aerosol particles.

2.3.2. Human nasal hairs

The physical properties of human nasal hair employed in the DEM model were obtained from open literature [4,5] and summarized in Table 2. Ma [4] has mentioned 2 hairs in each mm^2. Therefore, 262 hair strands in total have been created. The planted nasal hairs colored by their ID numbers can be found in Fig. 5. More details can be found in Section 2.1.1.

2.4. Boundary conditions

2.4.1. Nostril inlet condition

Constant inhalation flow rate inlet condition has been assigned to both nostrils (see Fig. 3 (a)). The inhalation flow rate employed in this study is from 216 mL/s to 630 mL/s, representing human nose breathing conditions from rest to exercise [4].

2.4.2. Nasopharynx outlet condition

Zero-gauge pressure outlet condition has been applied to the nasopharynx outlet (see Fig. 3 (a)).

2.4.3. Airway Wall condition

The nasal airway walls have been assigned a no-slip velocity boundary condition, assuming the airflow velocity at the wall is zero. Instead of using a 100% trapped wall boundary condition for particle-wall interaction, which assumes that a particle touching the airway wall is entrapped and does not re-enter the air stream [42], a more realistic particle deposition boundary condition was employed in this study. Specifically, the force balance of particles touching the airway wall was calculated using Eq. (9) to determine whether they will deposit on the wall or resuspend into the airflow. Specifically, the JKR surface energy between inhaled particles and airway walls is set to 5 J/m^2, validated by comparisons with experimental data (see Section 2.6). A smaller JKR surface energy value (1.29 J/m^2) has been utilized between spherical particles and between spherical particles and flexible fibers. This smaller value can account for the attachment and resuspension of inhaled aerosol on the nasal hairs.

2.5. Numerical setup

CFD simulations of nasal airflow dynamics were performed using Ansys Fluent 2022 R2 (Ansys Inc., Canonsburg, PA) on a local Dell Precision T7810 workstation (Intel® Xeon® Processor E5–2643 v4 with dual processors, 64 cores and 128 GB RAM). The transitional characteristics of the nasal airflow are modeled using k-ω SST model, which has been extensively validated in previous works [43–45]. The semi-implicit method for pressure-linked equations (SIMPLE) algorithm was employed for the pressure-velocity coupling, and the least-squares cell-

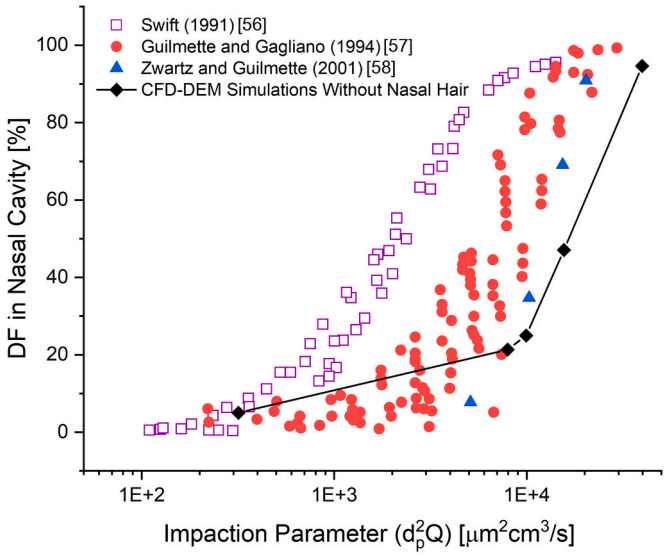

Fig. 6. Validation set for assessing the deposition fraction in the nasal cavity versus experimental data [56–58].

based scheme was applied to calculate the cell gradients. The second-order scheme was employed for pressure discretization. In addition, the second-order upwind scheme was applied for the discretization of momentum and turbulent kinetic energy. Convergence is defined for continuity, momentum, and supplementary equations when residuals are <1.0E-5.

Coupled with the CFD simulations mentioned above, DEM simulations of inhaled particle dynamics and nasal hair motion were performed using Ansys Rocky 2022 R2 (Ansys Inc., Canonsburg, PA) on local Dell Precision T7810 workstation (Intel® Xeon® Processor E5–2643 v4 with dual processors, 64 cores, and 128 GB RAM), Dell Precision 7920 Tower workstation (Intel® Xeon® Silver 4116 with dual processors and 128 GB RAM) with dual Quadro RTX 6000 GPUs, and the Ansys workstation (Intel® Xenon® CPU E5–2680 V3 @2.50GHz with 47 processors and NVIDIA Titan V100 GPUs).

It is worth noting that a two-way coupled CFD-DEM method was utilized to simulate the effect of nasal hair on the airflow field because the nasal hair acts as a barrier that obstructs the airflow. Therefore, it is necessary to account for the interactions between the airflow and the flexible nasal hairs to accurately simulate the flow patterns in the nasal cavity. On the other hand, a one-way coupled CFD-DEM method was applied for the simulation of the coarse dust particles. This is because the inhaled particle mass fraction was low in this study and their motion can be modeled as passive particles that move with the flow. The one-way coupled CFD-DEM model was constructed using the steady-state CFD data obtained from the two-way coupled CFD-DEM model at the point where the flexible fibers had reached an equilibrium state in terms of deformation.

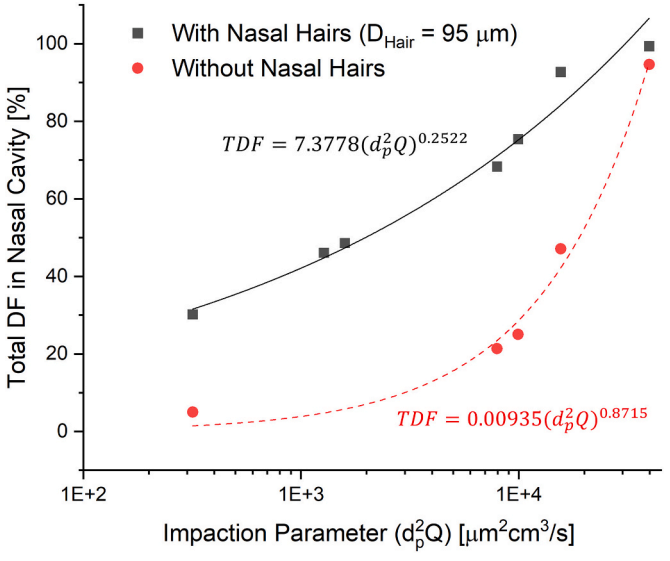

Fig. 7. Deposition fraction comparison between simulations with and without the nasal hairs.

Table 3
Deposition fractions (DFs) of the inhaled spherical particles on the nasal hairs and in the rest nasal cavity with three different nasal hair diameters under an selected inhalation flow rate (Q_{in} = 397.5 mL/s, and V_{air} = 5 m/s).

Hair Diameter [μm]	DF (Total) [%]	DF (Nasal Hairs) [%]	DF (Nasal Cavity) [%]
40	68.9669	11.7332	57.2337
95	78.6291	45.4666	33.1625
120	79.7167	49.2119	30.5048

2.6. Model validation

The accuracy of the CFD model on predicting airflow field in respiratory systems has been validated against benchmark experimental and numerical data, which are well documented in previous publications [46–55]. Since the DEM model is employed for predicting particle transport and deposition in the nasal cavity, extensive validations have been done on the accuracy of the particle depostion predictions by comparing the DEM results to in vitro data with various impaction parameter d_p^2Q [56–58], where Q is the average inhalation flow rate. For the DEM simulations used for model validation, inhalation flow rate is from 19.1 L/min to 23.85 L/min, and inhaled particle diameter is from 1 to 10 μm. Specifically, as shown in Fig. 6, without nasal hairs considered in either the in vitro experimental setup or the DEM simulations for validation, the DEM deposition fraction predictions show acceptable agreement with experimental data. Therefore, it can be confirmed that the particle-airway wall interaction boundary condition with surface energy equal to 5 J/m^2 can provide reasonably accurate predictions of inhaled particles.

3. Results and discussion

This study simulated inhaled air-particle transport dynamics through the nasal cavity with nasal hairs that have three different diameters ($D_{Hair} = 2r_\zeta$), i.e., 40, 95, and 120 μm. To quantify the nasal hair filtration efficiency, CFD-DEM simulations were also conducted with no nasal hair presence.

3.1. Influence of nasal hair presence on particle deposition in the nasal cavity

Fig. 7 visualized the influence of nasal hairs on the particle deposition predictions in the nasal cavity. It can be observed from both Table 3 and Fig. 7 that simulations with nasal hairs have higher total particle DFs in the nasal cavity than simulations without nasal hairs. This confirms the filtration efficiency of nasal hairs. In addition, it can be found that the DF differences in predictions between simulation cases with and without nasal hairs are higher than 20% for $3E+3 < d_p^2Q < 2E+4$ μm^{2}cm^3/s, which indicates that it is necessary to consider the influence of nasal hairs in CFD simulations of inhaled particle transport dynamics in the nasal cavity. It is worth noting that for high impaction parameter (i.e., $d_p^2Q = 4E+4$), the total DFs (TDFs) for simulations with and without nasal hairs ($D_{Hair} = 95$ μm as an example) are both very close to 100% due to the strong inertial impaction effect, which is the reason that

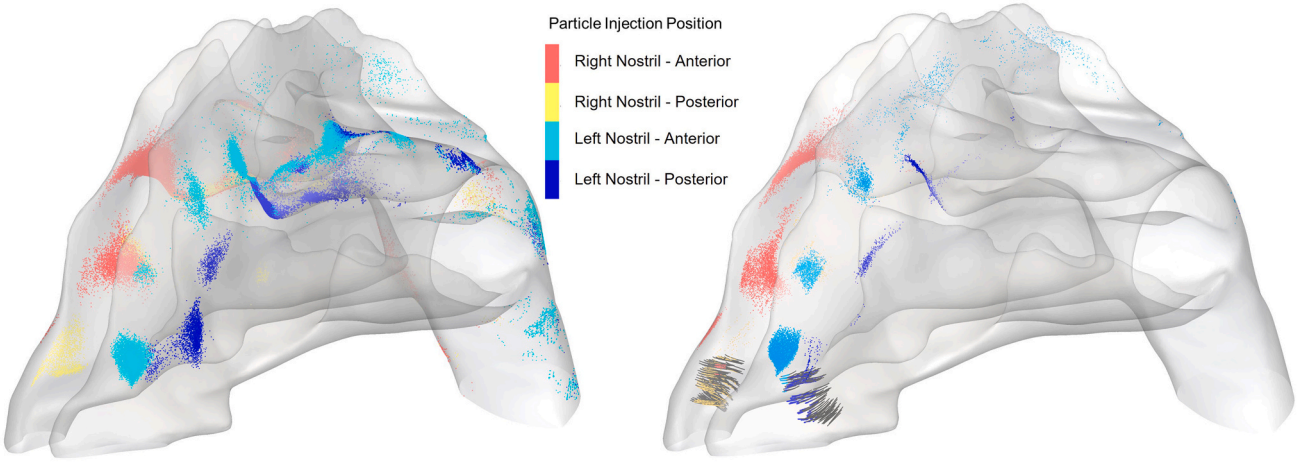

Fig. 8. Localized particle deposition patterns with and without nasal hairs (Q_{in}=397.5 mL/s, V_{air}=5 m/s, d_p=10 μm): (a) without nasal hair, and (b) with nasal hair (D_{Hair}=95 μm).

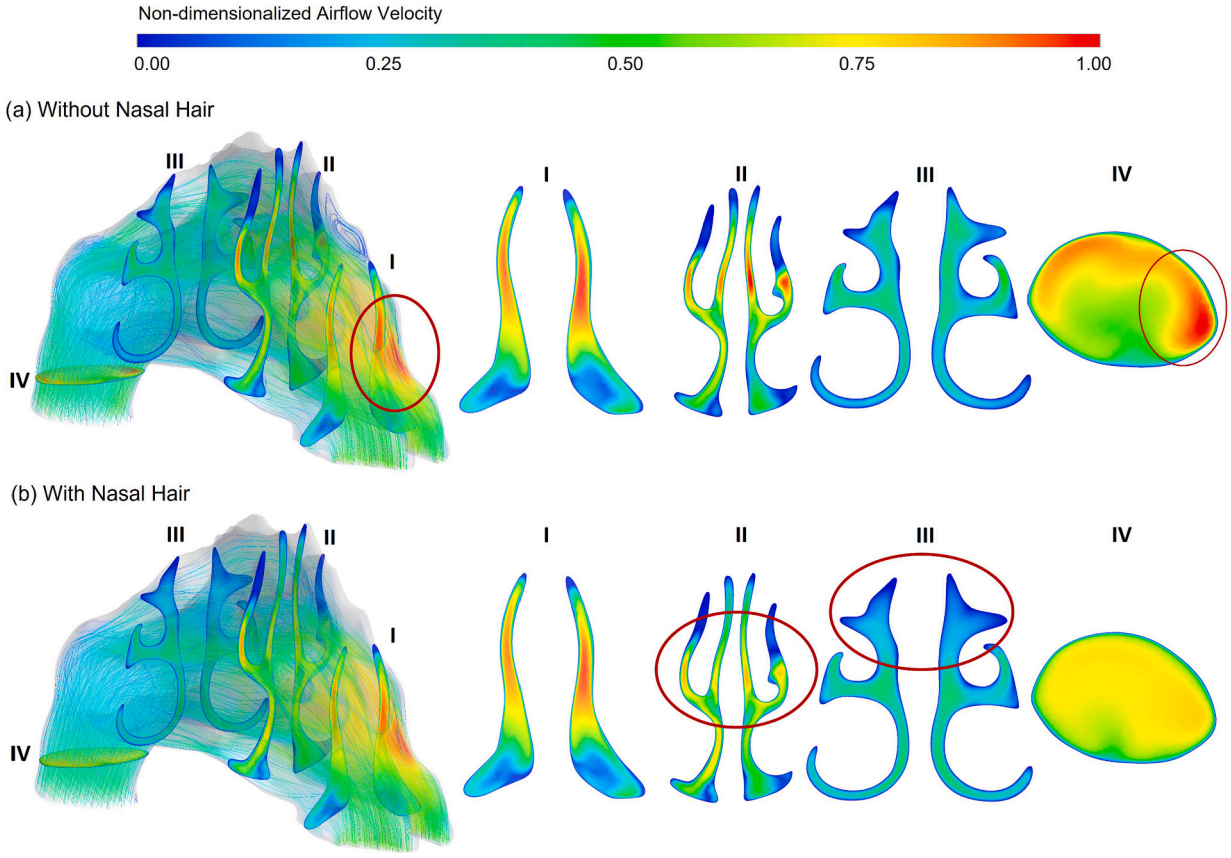

Fig. 9. Influence of nasal hair on airflow (Q_{in}=397.5 mL/s, V_{air}=5 m/s): (a) without nasal hair, and (b) without nasal hair (D_{Hair}=95 μm).

the difference in DF predictions is <3% (see Fig. 7). However, the localized particle deposition patterns are still with big differences (see Fig. 8 (a) and (b)). The simulation results show that the absence of nasal hair can cause more particles to deposit in the posterior region of the nasal cavity and nasopharynx (see Fig. 8 (a)) compared to the results with nasal hair (see Fig. 8 (b)). This highlights the importance of considering nasal hair presence for accurate delivery of inhaled therapeutic or toxic particles through simulations, even when d_p^2Q is high. Furthermore, the simulation results in Fig. 8 (a) and (b) demonstrate that nasal hair can effectively filter particles and prevent them from entering the nasopharynx.

3.2. Interactions between nasal hairs and nasal airflow

To quantify the influence of nasal hairs on inhaled air-particle dynamics in the nasal cavity, non-dimensionalized airflow velocity distributions were visualized and compared for simulations with and without nasal hairs (see Fig. 9 (a) and (b)). The inhalation flow rate Q_{in}=397.5 mL/s (i.e., V_{air}=5 m/s) and nasal hair diameter D_{Hair} = 95 μm were used

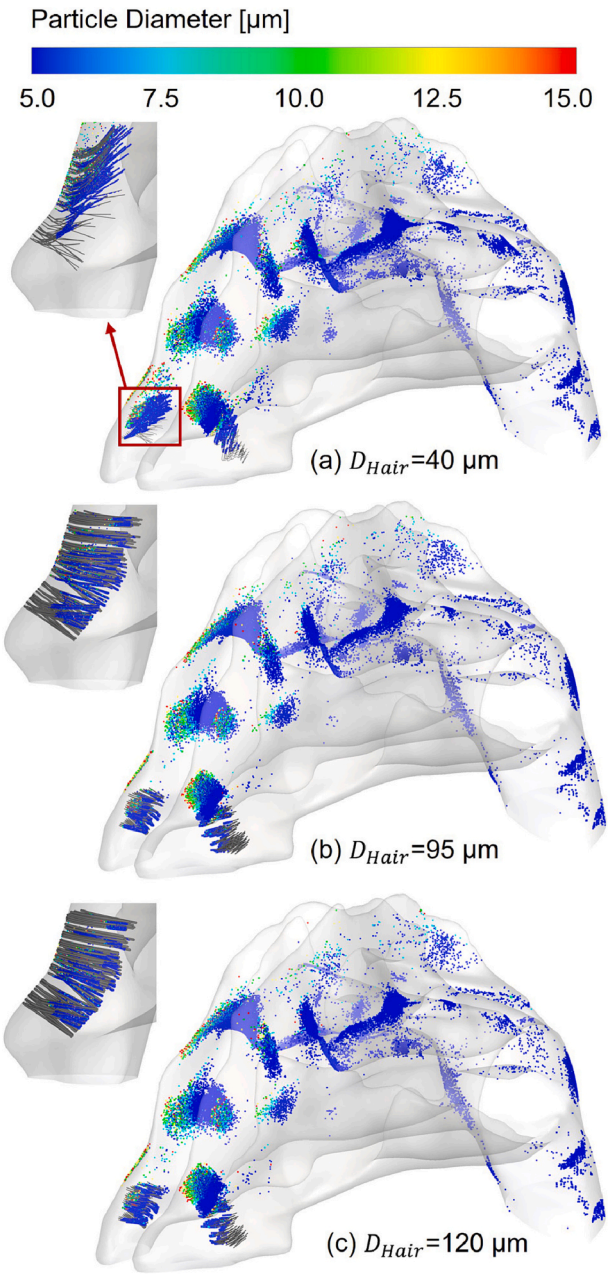

Fig. 10. Particle deposition with different nasal hair diameters (Q_{in}=397.5 mL/s, V_{air}=5 m/s).

as an example as shown in Fig. 9. Non-dimensionalized velocity was calculated by dividing the airflow velocity by the maximum velocity (9.24 m/s) in the computational domain, and the non-dimensionalized velocity ranges between 0 and 1. Airflow velocity visualizations were performed on four cross-sections (i.e., I, II, III, and IV). The results showed that the presence of nasal hairs resulted in more evenly distributed airflow through the inferior and middle turbinates (see the red circle on cross-section II in Fig. 9 (b)), but less airflow through the superior turbinate (see the red circle on cross-section III in Fig. 9 (b)). Additionally, the presence of nasal hairs led to more evenly distributed airflow in the nasopharynx (see the red circle on cross-section IV in Fig. 9 (b)). Thus, it can be concluded that nasal hairs have a considerable influence (24.7% difference in the maximum local velocity on cross-section IV) on airflow distributions in the nasal cavity, and it is necessary to model nasal hair presence in CFD simulations to obtain more physiologically realistic airflow distribution predictions.

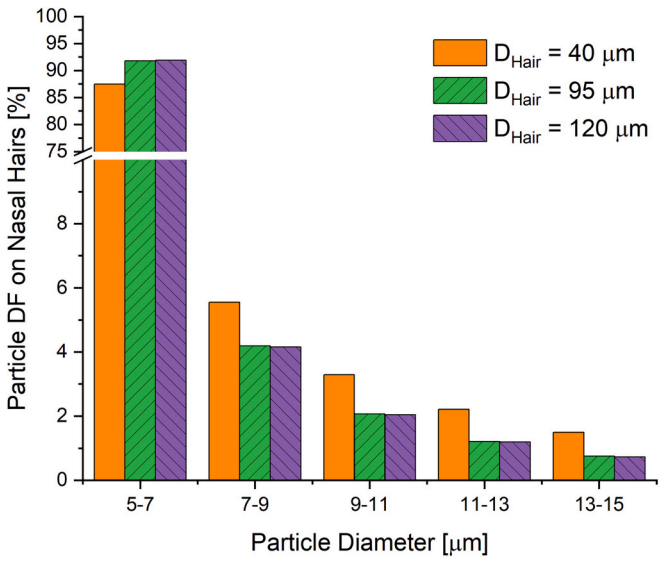

Fig. 11. Size distribution of particles trapped on nasal hairs with different diameters (Q_{in}=397.5 mL/s, V_{air}=5 m/s).

3.3. Particle deposition vs. nasal hair diameter

Table 3 and Fig. 10 present the DFs and particle local deposition patterns in the nasal cavity with nasal hairs that have different hair diameters (D_{Hair}= 40, 95, and 120 μm). It can be found in Table 3 that thicker nasal hairs with higher D_{Hair} can trap more particles than thinner nasal hairs for the particle size distributions employed in this study (see Section 2.3.1), of which most particles are approximately 5 μm in diameter. Accordingly, Table 3 also shows that with the increase in D_{Hair}, particles deposited on the nasal cavity wall decreases. This is due to the more effective filtration with the thicker nasal hair than the thinner ones. Due to the particle sizes selected in this study (see Fig. 4), the main deposition mechanisms are inertial impaction and interception. Brownian motion induced deposition on nasal hair can be neglected. The D_{Hair} influence on filtration efficiency is due to the following shifts in the interactions between inhaled air-particle flow and the nasal hairs with different D_{Hair} values. Firstly, thinner nasal hairs with smaller D_{Hair} is more flexible than thicker nasal hairs. This is because of the reduced stiffness of particles with smaller diameter (see Eq. (4)). As shown in Fig. 10, thinner nasal hairs deformed more (see Fig. 10 (a)) than thicker nasal hairs (see Fig. 10 (c)) subject to the hydraulic forces and contact forces given by the inhaled air and particles. The higher bending motion of the thinner hairs give higher openings in the nasal airway passages, which allows more particles penetrate through the nasal vestibule without being trapped due to the interception by the nasal hairs. In addition, the higher mobility of the thinner nasal hairs also leads to higher chance for the deposited particles on the nasal hairs to be resuspended into the air. Secondly, with the same number of nasal hairs, thinner hairs occupy less cross-section areas in the nasal vestibule than thicker hairs, which also lead to lower filtration capability due to the lower chance to lead to particle deposition due to interception. Fig. 11 visualize the particle DFs on nasal hairs with different D_{Hair} and particle sizes, using inhalation flow rate Q_{in}=397.5 mL/s (i.e., V_{air}=5 m/s) as an example. For particles between 5 and 7 μm, the nasal hair filtration efficiency increases with the D_{Hair}, which aligned with the observation in Table 3 for the polydisperse particles inhaled. However, it is very interesting that for particles larger than 7 μm, the filtration efficiency of nasal hairs decreases with the increase in D_{Hair}. The reason for this is that when larger particles collide with nasal hairs, they have a greater impact force which can vibrate the nasal hairs and reduce the efficiency of nasal hairs in filtering out particles. In contrast to the noticeable differences in DFs included by nasal hairs with different D_{Hair}, no significant deposition

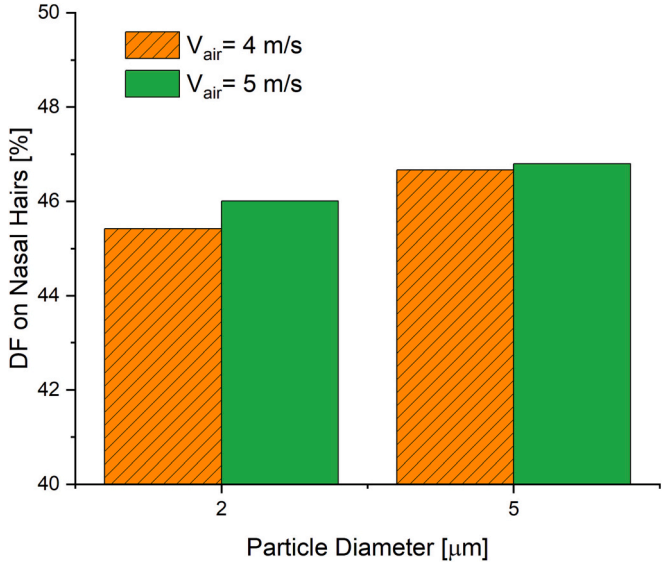

Fig. 12. Inhalation flow rate influence on particle DF on nasal hairs (D_{Hair}=95 μm).

distributions were found among Figs. 10 (a) – (c).

3.4. Particle deposition on nasal hairs vs. particle size

Fig. 11 illustrates that as particle diameters increase from 5 μm to 15 μm, a smaller percentage of particles are trapped by nasal hairs. This is primarily due to the enhanced inertial effects and the higher initial momentum carried by larger particles, which cannot be sufficiently dissipated by the nasal hairs for effective trapping. Interestingly, nasal hairs exhibit remarkable filtration efficiency for smaller particles between 5 and 7 μm. Although larger particles are not effectively trapped by nasal hairs, most still deposit in the nasal vestibule (see Fig. 10) with highly concentrated deposition patterns, owing to their strong inertial impaction effect. This indicates a limited ability for larger particles to travel into the nasal cavity and nasopharynx and enter the tracheobronchial tree. In contrast, smaller particles that travel beyond the nasal vestibule display more dispersed deposition patterns within the nasal cavity. As these particles can more easily reach the olfactory region and other anterior nasal cavity regions, they have a higher potential to be therapeutically or toxically effective by passing through the blood-brain barrier, to treat neurodegenerative diseases such as Alzheimer's and Parkinson's, as well as causing more serious neurological disorders [59,60].

3.5. Particle deposition vs. inhalation flow rate

Figs. 12 and 13 show the influence of inhalation flow rate on airflow field distribution, particle DFs and location deposition patterns on nasal hairs, as well as the non-dimensionalized hydraulic forces acting on nasal hairs. D_{Hair}=95 μm was selected as the example. Specifically, the non-dimensionalized hydraulic force is equal to the local hydraulic force acting on fibers (i.e., drag force $\vec{F}_{f,\zeta}$ in Eq. (1)) divided by the maximum drag force magnitude (2.1E-5 N) in the computational domain. As shown in Fig. 12, for 2-μm and 5-μm particles, increasing inhalation flow rate Q_{in} from 318 mL/s to 397.5 mL/s (i.e., inhalation airflow velocity V_{air} from 4 m/s to 5 m/s) leads to increased DF of particles on nasal hairs. Due to the similar deformation of nasal hairs shown in Figs. 13 (a) and (b), as well as the less scattered particle deposition patterns on nasal hairs with higher Q_{in} (i.e., less particle deposition on posterior nasal hairs in Fig. 13 (b) compared to Fig. 13 (a)), it suggests that the increase

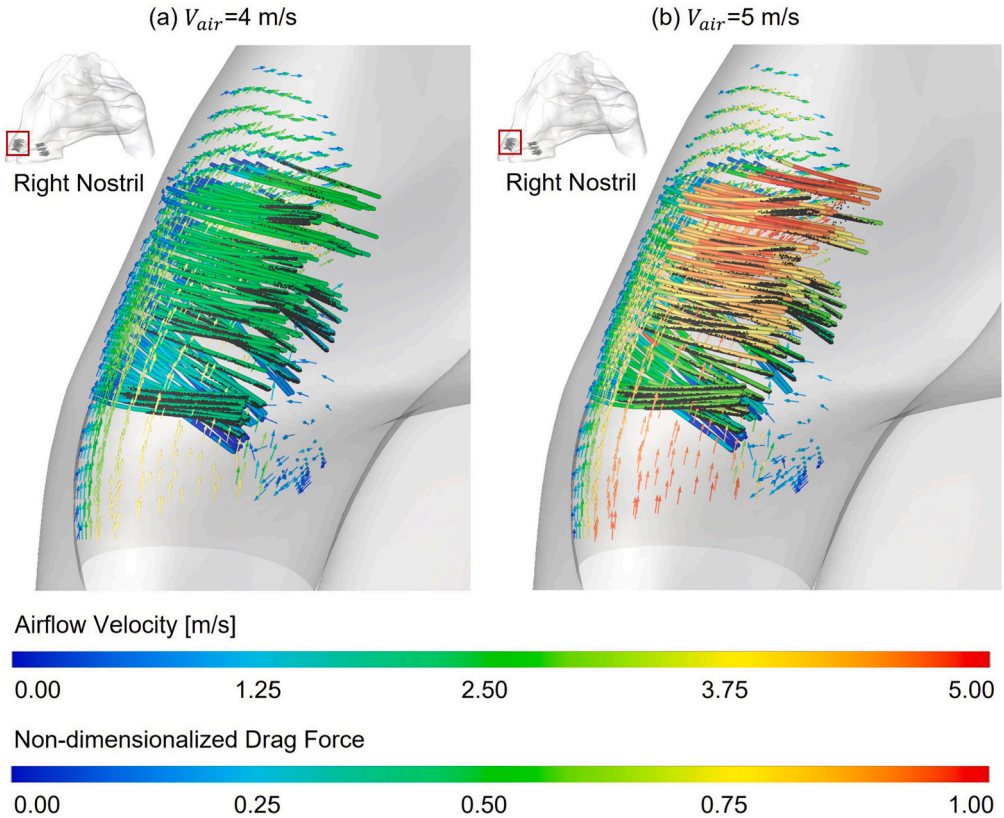

Fig. 13. Inhalation flow rate influence on nasal hair deformation, airflow field, and particle deposition on nasal hairs (D_{Hair}=95 μm): (a) Q_{in}=318 mL/s, V_{air}=4 m/s, and (b) Q_{in}=397.5 mL/s, V_{air}=5 m/s.

in particle DF shown in Fig. 12 is due to the enhanced inertial impaction induced by the higher inhalation flow rate for 2-μm and 5-μm particles. However, it is important to note that the influence of inhalation flow rate on particle deposition may differ for smaller D_{Hair}. Smaller D_{Hair} reduces the stiffness of nasal hairs, which means they will deform more under higher inhalation flow rates. This is not reflected in Figs. 13 (a) and (b), but is similar to what is shown in Fig. 10 (a). It is hypothesized that different deformation of nasal hairs due to changes in flow rate may induce more complex shifts in particle DF on nasal hairs, requiring further investigation in the future. Additionally, Figs. 13 (a) and (b) also show the airflow velocity vectors in the near field of the nasal hairs. The velocity vector fields are similar to each other with a slightly increased flow rate, except for the magnitude of the non-dimensionalized velocity.

4. Conclusions

This study developed a first-of-its-kind CFD-DEM model and investigated the influence of nasal hairs on inhaled air-particle dynamics in a nasal cavity. Key conclusions are summarized below, i.e.,

(1) Nasal hairs have a significant influence on airflow distributions in the nasal cavity, and it is necessary to model nasal hair presence in CFD simulations to obtain more physiologically realistic airflow distribution predictions;
(2) Simulations with nasal hairs have higher total particle deposition fractions in the nasal cavity than simulations without nasal hairs, confirming the filtration efficiency of nasal hairs;
(3) Thicker nasal hairs with higher diameters can trap more particles than thinner nasal hairs, and the filtration efficiency of nasal hairs increases with the nasal hair diameter for particles between 5 and 7 μm;
(4) Nasal hairs demonstrate significant filtration efficiency for smaller particles ranging from 5 to 7 μm. However, larger particles are not effectively captured by nasal hairs and instead tend to deposit in the nasal vestibule, exhibiting concentrated deposition patterns. This phenomenon can be attributed to the higher momentum of larger particles upon impacting the nasal hairs, which subsequently increases their probability of resuspension after colliding with the nasal hairs;
(5) Smaller nasal hair diameter reduces the stiffness of nasal hairs, and it is hypothesized that the different deformation of nasal hairs due to changes in flow rate may induce more complex shifts in particle deposition on nasal hairs; and
(6) Nasal hairs have a significant influence on non-dimensionalized hydraulic forces acting on fibers, and increasing inhalation flow rate leads to increased DF of particles on nasal hairs for 2-μm and 5-μm particles due to enhanced inertial impaction.

4.1. Limitations of this study and future work

Despite the improved modeling capability of interactions between nasal hairs and inhaled air-particle flow results obtained from the CFD-DEM model, there are several limitations in the current study, i.e.,

(1) The computational domain of the nasal cavity did not include sinuses (i.e., sphenoid, ethmoid, frontal, and maxillary sinuses);
(2) Mucus presence and its clearance mechanisms were not modeled;
(3) Steady-state inhalation velocity was employed, rather than the more physiologically realistic transient inhalation-exhalation profiles;
(4) The influence of nasal hair number density (i.e., hair count per unit area) and nasal hair length were not investigated;
(5) Particles with diameters <5 μm, including PM2.5, were not modeled in this study; and
(6) This study was limited by the utilization of only one subject-specific nasal cavity geometry, which restricts the generalizability of the findings to different population groups.

Future work will be conducted to address these limitations by

(1) Incorporating sinuses into the nasal cavity computational domain for a more comprehensive analysis;
(2) Modeling the presence of mucus and its clearance mechanisms to account for their effects on particle deposition and transport;
(3) Utilizing transient inhalation-exhalation profiles to better represent physiological breathing conditions;
(4) Investigating the influence of nasal hair number density and length on particle transport and deposition dynamics;
(5) Extending the particle size range to include smaller particles such as PM2.5, to better understand their behavior and potential health effects; and
(6) Incorporating a broader range of subject-specific nasal cavity geometries to capture the anatomical variations among individuals.

CRediT authorship contribution statement

Ahmadreza Haghnegahdar: Conceptualization, Methodology, Software, Validation, Visualization, Formal analysis, Data curation, Writing – original draft, Writing – review & editing. **Rahul Bharadwaj:** Conceptualization, Software, Supervision. **Yu Feng:** Conceptualization, Supervision, Data curation, Visualization, Writing – original draft, Writing – review & editing, Funding acquisition.

Declaration of Competing Interest

The authors declare that they have no known competing financial interests or personal relationships that could have appeared to influence the work reported in this paper.

Data availability

The data that support the findings of this study are available from the corresponding author upon reasonable request.

Acknowledgment

This material is based upon work supported by the National Science Foundation under grant no. CBET 2120688. The use of Ansys Rocky and Ansys Fluent (Ansys Inc., Canonsburg, PA) as part of the Ansys-CBBL academic partnership is also gratefully acknowledged.

Appendix A. Supplementary data

Supplementary data to this article can be found online at https://doi.org/10.1016/j.powtec.2023.118710.

References

[1] C.T. Pham, et al., Measurement and quantification of cadaveric nasal hairs, Int. J. Dermatol. 61 (11) (2021) e456–e457.
[2] A. Ozturk, et al., Does nasal hair (vibrissae) density affect the risk of developing asthma in patients with seasonal rhinitis? Int. Arch. Allergy Immunol. 156 (1) (2011) 75–80.
[3] D.G. Stoddard Jr., J.F. Pallanch, G.S. Hamilton, The effect of vibrissae on subjective and objective measures of nasal obstruction, Am. J. Rhinol. Allergy 29 (5) (2015) 373–377.
[4] C.-J. Ma, Experimental verification of the particle blocking feature of nasal hair, Asian J. Atmos. Environ. (AJAE) 13 (2) (2019).
[5] P. GS, M. CD, On the Pullout Strength of Human Nasal Hair (Vibrissae), 2023. Available at SSRN 3552446.
[6] M. Gao, X. Shen, S. Mao, Factors influencing drug deposition in the nasal cavity upon delivery via nasal sprays, J. Pharm. Investig. 50 (3) (2020) 251–259.
[7] K. Inthavong, et al., Optimising nasal spray parameters for efficient drug delivery using computational fluid dynamics, Comput. Biol. Med. 38 (6) (2008) 713–726.

[8] M. Kiaee, et al., Regional deposition of nasal sprays in adults: a wide ranging computational study, Int. J. Numer. Methods Biomed. Eng. 34 (5) (2018), e2968.
[9] O. Pourmehran, et al., Acoustic drug delivery to the maxillary sinus, Int. J. Pharm. 606 (2021), 120927.
[10] Y. Shang, et al., Prediction of nasal spray drug absorption influenced by mucociliary clearance, PLoS One 16 (1) (2021), e0246007.
[11] S. Vachhani, C. Kleinstreuer, Comparison of micron-and nano-particle transport in the human nasal cavity with a focus on the olfactory region, Comput. Biol. Med. 128 (2021), 104103.
[12] H. Calmet, et al., Subject-variability effects on micron particle deposition in human nasal cavities, J. Aerosol Sci. 115 (2018) 12–28.
[13] J. Xi, P.W. Longest, Numerical predictions of submicrometer aerosol deposition in the nasal cavity using a novel drift flux approach, Int. J. Heat Mass Transf. 51 (23–24) (2008) 5562–5577.
[14] T. Radulesco, et al., Functional relevance of computational fluid dynamics in the field of nasal obstruction: a literature review, Clin. Otolaryngol. 44 (5) (2019) 801–809.
[15] N.P. Singh, K. Inthavong, Can computational fluid dynamic models help us in the treatment of chronic rhinosinusitis, Curr. Opin. Otolaryngol. Head Neck Surg. 29 (1) (2021) 21–26.
[16] G. Maza, et al., Computational fluid dynamics after endoscopic endonasal skull base surgery—Possible empty nose syndrome in the context of middle turbinate resection, in: International Forum of Allergy & Rhinology, Wiley Online Library, 2019.
[17] T. Crosby, et al., Computational fluid dynamics model of laryngotracheal stenosis and correlation to pulmonary function measures, Respir. Physiol. Neurobiol. 312 (2023), 104037.
[18] H. Li, et al., A CFD Study of Fluid-Particle Behaviour in a Porous Vestibule of a Human Nasal and Pharynx Airway, 2006.
[19] D.-J. Hsu, M.-H. Chuang, In-vivo measurements of micrometer-sized particle deposition in the nasal cavities of Taiwanese adults, Aerosol Sci. Technol. 46 (6) (2012) 631–638.
[20] X. Chen, et al., CFD–DEM simulation of particle transport and deposition in pulmonary airway, Powder Technol. 228 (2012) 309–318.
[21] J. Zhao, et al., Prediction of the carrier shape effect on particle transport, interaction and deposition in two dry powder inhalers and a mouth-to-G13 human respiratory system: a CFD-DEM study, J. Aerosol Sci. 160 (2022), 105899.
[22] Y. Feng, C. Kleinstreuer, Micron-particle transport, interactions and deposition in triple lung-airway bifurcations using a novel modeling approach, J. Aerosol Sci. 71 (2014) 1–15.
[23] Y. Guo, et al., A bonded sphero-cylinder model for the discrete element simulation of elasto-plastic fibers, Chem. Eng. Sci. 175 (2018) 118–129.
[24] A.A. Adebiyi, J.F. Kok, Climate models miss most of the coarse dust in the atmosphere, Sci. Adv. 6 (15) (2020) p. eaaz9507.
[25] H. Shi, C. Kleinstreuer, Z. Zhang, Modeling of inertial particle transport and deposition in human nasal cavities with wall roughness, J. Aerosol Sci. 38 (4) (2007) 398–419.
[26] H.R. Norouzi, et al., Coupled CFD-DEM Modeling: Formulation, Implementation and Application to Multiphase Flows, John Wiley & Sons, 2016.
[27] M. Jiang, et al., Experimental and DEM analyses on wheel-soil interaction, J. Terrramech. 76 (2018) 15–28.
[28] K.L. Johnson, et al., Surface energy and the contact of elastic solids, Proc. R. Soc. Lond. A 324 (1558) (1971) 301–313.
[29] N. Marheineke, R. Wegener, Modeling and application of a stochastic drag for fibers in turbulent flows, Int. J. Multiphase Flow 37 (2) (2011) 136–148.
[30] S. Ergun, Fluid flow through packed columns, Chem. Eng. Prog. 48 (2) (1952) 89–94.
[31] C.Y. Wen, Mechanics of fluidization. In fluid particle technology, Chem. Eng. Prog. Symp. Ser. 62 (1966) 100–111.
[32] Y. Shimazaki, et al., Three-dimensional numerical simulation of nanoparticle inhalation and indoor pollution around breathing human, J. Environ. Eng. 4 (1) (2009) 145–161.
[33] R.W. Johnson, Handbook of Fluid Dynamics, Crc Press, 2016.
[34] P. Saffman, The lift on a small sphere in a slow shear flow, J. Fluid Mech. 22 (2) (1965) 385–400.
[35] A. Li, G. Ahmadi, Deposition of aerosols on surfaces in a turbulent channel flow, Int. J. Eng. Sci. 31 (3) (1993) 435–451.
[36] E. Cunningham, On the velocity of steady fall of spherical particles through fluid medium, Proc. R. Soc. Lond. Ser. A 83 (563) (1910) 357–365.
[37] H. Hertz, Ueber die Berührung fester elastischer Körper, 1882.
[38] A.O. Raji, Discrete Element Modelling of the Deformation of Bulk Agricultural Particulates, Newcastle University, 1999.
[39] Y. Tsuji, T. Kawaguchi, T. Tanaka, Discrete particle simulation of two-dimensional fluidized bed, Powder Technol. 77 (1) (1993) 79–87.
[40] R.D. Mindlin, H. Deresiewicz, Elastic spheres in contact under varying oblique forces, J. Appl. Mech. 20 (3) (1953) 327–344.
[41] G. Tian, et al., Validating CFD predictions of pharmaceutical aerosol deposition with in vivo data, Pharm. Res. 32 (10) (2015) 3170–3187.
[42] J. Zhao, et al., Prediction of airway deformation effect on pulmonary air-particle dynamics: a numerical study, Phys. Fluids 33 (10) (2021), 101906.
[43] Y. Feng, C. Kleinstreuer, Analysis of non-spherical particle transport in complex internal shear flows vol. 25, 2013, p. 1904.
[44] Y. Feng, et al., An in silico inter-subject variability study of extra-thoracic morphology effects on inhaled particle transport and deposition, J. Aerosol Sci. 123 (2018) 185–207.
[45] Z. Zhang, C. Kleinstreuer, S. Hyun, Size-change and deposition of conventional and composite cigarette smoke particles during inhalation in a subject-specific airway model, J. Aerosol Sci. 46 (2012) 34–52.
[46] Y. Feng, C. Kleinstreuer, Analysis of non-spherical particle transport in complex internal shear flows, Phys. Fluids 25 (9) (2013), 091904.
[47] Y. Feng, et al., Computational transport, phase change and deposition analysis of inhaled multicomponent droplet–vapor mixtures in an idealized human upper lung model, J. Aerosol Sci. 96 (6) (2016) 96–123.
[48] Y. Feng, C. Kleinstreuer, A. Rostami, Evaporation and condensation of multicomponent electronic cigarette droplets and conventional cigarette smoke particles in an idealized G3–G6 triple bifurcating unit, J. Aerosol Sci. 80 (2015) 58–74.
[49] Y. Feng, et al., Influence of wind and relative humidity on the social distancing effectiveness to prevent COVID-19 airborne transmission: a numerical study, J. Aerosol Sci. 147 (2020) 105585.
[50] Y. Feng, et al., Tutorial: understanding the transport, deposition, and translocation of particles in human respiratory systems using computational fluid-particle dynamics and physiologically based Toxicokinetic models, J. Aerosol Sci. 151 (2021), 105672.
[51] A. Haghnegahdar, et al., Computational analysis of deposition and translocation of inhaled nicotine and acrolein in the human body with e-cigarette puffing topographies, Aerosol Sci. Technol. 52 (5) (2018) 483–493.
[52] A. Haghnegahdar, J. Zhao, Y. Feng, Lung aerosol dynamics of airborne influenza a virus-laden droplets and the resultant immune system responses: an in silico study, J. Aerosol Sci. 134 (2019) 21.
[53] J. Zhao, et al., Numerical simulation of welding fume lung dosimetry, J. Aerosol Sci. 135 (2019) 113–129.
[54] J.F. Zhao, C. Fromen, Glottis motion effects on the inhaled particle transport and deposition in a subject-specific mouth-to-Trachea model: an CFPD study, Comput. Biol. Med. (2020) 116.
[55] J.F. Zhao, A. Haghnegahdar, S. Sarkar, R. Bharadwaj, Numerical investigation of particle shape and actuation flow rate effects on lactose carrier delivery efficiency through a dry powder inhaler (DPI) using CFD-DEM, in: 2020 Virtual AIChE Annual Meeting 2020, 2020.
[56] D. Swift, Inspiratory inertial deposition of aerosols in human nasal airway replicate casts: implication for the proposed NCRP lung model, Radiat. Prot. Dosim. 38 (1–3) (1991) 29–34.
[57] R. Guilmette, T. Gagliano, Construction of a model of human nasal airways using in vivo morphometric data, Ann. Occup. Hyg. 38 (inhaled_particles_VII) (1994) 69–75.
[58] G. Zwartz, R. Guilmette, Effect of flow rate on particle deposition in a replica of a human nasal airway, Inhal. Toxicol. 13 (2) (2001) 109–127.
[59] M. Agrawal, et al., Nose-to-brain drug delivery: an update on clinical challenges and progress towards approval of anti-Alzheimer drugs, J. Control. Release 281 (2018) 139–177.
[60] V.S. Tambe, S. Wairkar, Lipid-based Nanocarriers via nose-to-brain pathway for Alzheimer's and Parkinson's disease, Curr. Nanosci. 19 (3) (2023) 322–337.
[61] J.T. Hansen, Netter's Clinical Anatomy-E-Book, Elsevier Health Sciences, 2021.